Tests of EXAFS on OMEGA: Feasibility for Shock-Heating Measurements

Introduction

As part of its participation in the Stockpile Stewardship Program (SSP), LLE is studying the feasibility of using extended x-ray absorption fine structure (EXAFS)[1] to characterize the properties of solid materials shocked at moderately high pressures (up to a few megabars). In particular, there is an interest in examining material properties since they affect the growth of hydrodynamic instabilities. Thus, a shocked material that retains its strength (or shear) will be more resistant to such instabilities than a molten solid. EXAFS is sensitive to the short-range order in crystals (as opposed to diffraction, which depends on longer-range order). It can be seen in amorphous materials[2,3] as well as liquids,[4–6] but the reduction in short-range order due to melting is then evident in the EXAFS spectrum. EXAFS can measure the density and temperature of the shocked solid in addition to indicating melting. The main limitation in shock-heating studies is the reduction of the EXAFS modulation amplitude with increasing temperature. This problem is discussed in detail in this article. EXAFS can possibly indicate whether the shock compression of the solid is one- or three-dimensional: the distances to the nearest atomic neighbors (which is measured by EXAFS) are different in the two cases. Initial tests show very high contrast EXAFS modulations when a thick, undriven Ti foil is backlit by the x-ray radiation from an imploded CH shell. The high contrast achieved in these tests is due to three factors: (a) using an imploded target as a backlighter, (b) using a very thick Ti absorber, and (c) using a CID array for detection. In preparation for future shocked-Ti experiments, we scope out the range of shock strengths where significant EXAFS modulation can be expected. Briefly, although a higher temperature reduces the amplitude of EXAFS modulations, a higher density mitigates this reduction (by raising the Debye temperature). For varying shock strengths we determine the temperature and density of the Ti metal and then the expected EXAFS visibility. EXAFS has been previously seen in laser-produced plasma experiments,[7] and at LLE it has been studied[8] in imploded spherical targets (where the absorber was also Ti).

Experiment

The tests reported here were performed with undriven, 12.5-μm-thick Ti foils, positioned in front of an x-ray spectrometer. Such tests are useful for determining the ability of the diagnostic system to measure the high-quality EXAFS modulations required to analyze shock-heated materials. The last section of this article discusses the problem of EXAFS visibility in future shocked-Ti experiments. In the present experiment, the 60-beam OMEGA laser system with SSD-smoothed beams (1.5 × 11-Å bandwidth) was used to implode CH shells. We show data from two almost identical shots (21238 and 21239), where a 1-ns square pulse of energy ~22.8 kJ was used to implode 20-μm-thick CH shells of 937-μm outer diameter, filled with a mixture of hydrogen at 2.4 atm and deuterium at 0.6 atm.

Figure 86.50 shows the spectrum from shot 21238 obtained when the radiation emitted by the imploding CH shell is transmitted through the 12.5-μm-thick Ti foil and measured by a Ge(1,1,1) crystal and a CID array (see below). The EXAFS modulations above the Ti *K* edge are clearly seen. The high-contrast modulations are due to three factors employed in these tests:

(a) Using the intense (and smooth) emission of an imploding CH target as a backlighter. The smoothness of the incident spectrum is important for measuring modulations in the absorption. In other applications, a high-*Z* planar target is typically used for backlighting because it generates a line spectrum. The compressed CH, on the other hand, produces a smooth continuum spectrum; the high radiation intensity (~10^{17} keV/keV at 5 keV) is due to the high density, not the high *Z*. Additional advantages of the imploded backlighter are the short emission time, ~120 ps (which may yield useful results even without time resolution), and the small dimension, leading to higher spectral resolution.

(b) Using a thick Ti foil, which results in a very high attenuation, ~exp(−4), rather than the customary attenuation of ~exp(−1). This increases the relative modulations in the measured signal: if the latter is written as $I \sim \exp(-\tau d)$, where τ is the opacity and d is the foil thickness, the relative modulation $|\Delta I/I| \sim d\Delta\tau$ is proportional to the foil thickness. The optimal thickness is the largest for which the signal is still above the noise level. The choice of 12.5-μm thickness is possible due to the high intensity of the flux from an imploded target. We show below that measuring an EXAFS spectrum through such a thick foil does not detract from our ability to study shocks launched into the foil. Specifically, the shock is quite uniform when its front has reached the back of the foil. This is important for an unambiguous interpretation of the absorption results. The choice of titanium (rather than a lower-Z foil) results from the fact that with a high attenuation the detected spectrum is dominated by the second-order crystal diffraction (for which the attenuation is much smaller). In Ti the second-order radiation (around ~10 keV) is too weak to affect the results.

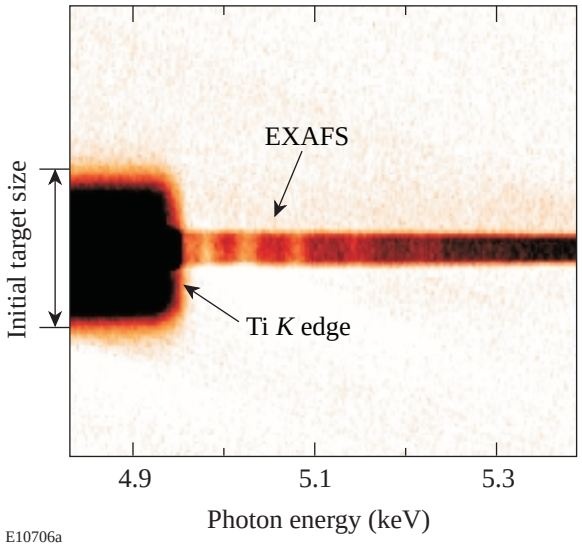

Figure 86.50
EXAFS modulation spectrum obtained on a CID array (shot 21238) when the x rays from an OMEGA-imploded CH target are absorbed by a 12.5-μm-thick Ti foil. Below the K edge the radiation from the entire target is strong enough to be seen; above the K edge only radiation from the compressed core is seen.

(c) Using CID electronic detection rather than film. The CID array we used (from CID Technologies, Inc.) was an 812 × 604 array having square pixels with 38.5-μm center-to-center spacing, uncooled and with no conversion phosphor. The analog-to-digital converter with 16-bit resolution was fast enough to minimize the effect of dark current. The superior performance with respect to film is mainly due to the lower noise. CID arrays are more immune to radiation damage than CCD arrays; they have been extensively studied, implemented, and calibrated at LLE.[9]

The spectrum in Fig. 86.50 is spatially resolved in the vertical direction. Above the K edge, because of the strong attenuation, only the more intense radiation from the compressed core can be seen. Below the K edge the intensity is high enough to be seen over the whole target volume (and to saturate the core image). The spectrum without the absorber (i.e., the incident spectrum) is measured in parallel by employing additional filtering.

Figure 86.51 is a lineout through the calibrated spectrum, and it shows that the depth of modulation is indeed high. The choice of Ti foil thickness is about optimal for the available x-ray flux, as seen from the fact that the minimum intensity is close to zero.

The theory of EXAFS[1] yields an expression for $\chi(k) = \mu(k)/\mu_0(k) - 1$, where $\mu(k)$ is the absorption coefficient (or opacity) and $\mu_0(k)$ is the absorption of the isolated atom (i.e.,without the EXAFS oscillations). By passing a smooth curve through the EXAFS oscillations, $\mu_0(k)$ can be obtained (it is also known from published tables). The wave number k of the ejected photoelectron is given by $\hbar^2 k^2/2m = E - E_K$, where E is the absorbed photon energy and E_K is the energy of the K edge. Figure 86.52 shows the quantity $\chi(k)$ derived from Fig. 86.51. The period and magnitude of the oscillations agree well with what is obtained in synchrotron experiments on Ti,[10] but the first peak is too high in comparison.

To assess the noise in the measured spectrum we compare successive spectra in adjacent rows of pixels (horizontal rows in Fig. 86.50). If S_i is the signal (or spectrum) of the ith row, the average signal S (such as was used in Fig. 86.51) is given by

$$S = \sum_{i=1}^{m} S_i/m, \qquad (1)$$

where we select m central rows within the spatial (vertical) profile to avoid edge effects. For the average noise N, using the same rows, we write

$$N = \sum_{i=1}^{m/2} \left(S_{2i-1} - S_{2i}\right)/m. \quad (2)$$

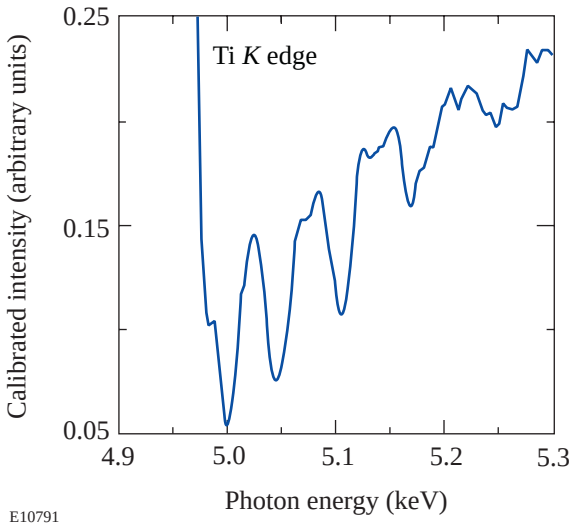

Figure 86.51
The calibrated EXAFS signal for shot 21238 in arbitrary units. The relative depth of modulation is seen to be very high.

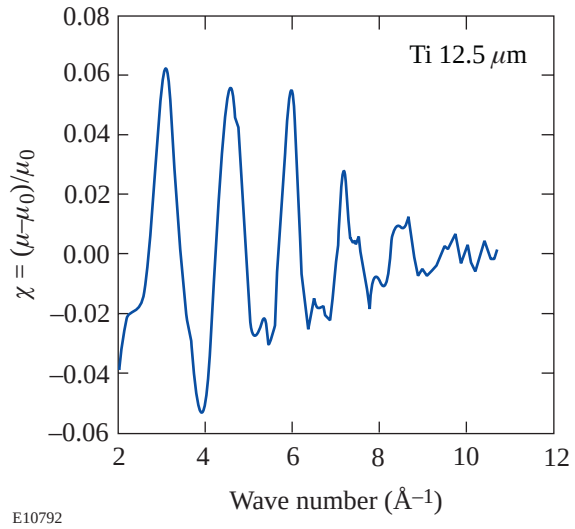

Figure 86.52
Measured relative modulation of the absorption in Ti derived from Fig. 86.51 as a function of the wave number of the ejected electron (following K-shell photoionization).

The random components of the measured signal add up in Eq. (2), whereas the net signal cancels out; thus, N is the appropriate noise quantity to be compared with S. Figure 86.53 compares the signal (above the K edge) and the noise in the same units (pixel values). The signal is taken to be the modulations in Fig. 86.51 around a smooth average curve [the subtraction in Eq. (2) cancels out both this smooth curve and the EXAFS modulation around it]. The noise is seen to be negligible relative to the signal up to k ~10.5 Å^{-1}, beyond which the data is ignored.

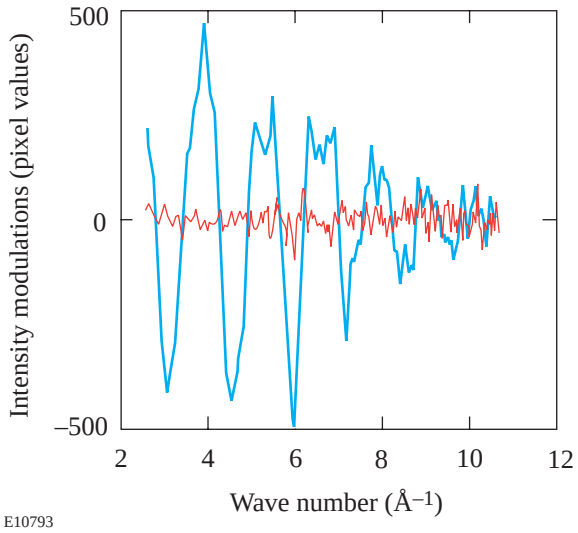

Figure 86.53
Comparison of the EXAFS signal and noise using the results of Fig. 86.50 and Eqs. (1) and (2). The signal is given by the modulations in Fig. 86.51 around a smooth average curve.

Theory of EXAFS

When photons of energy above the K edge (say, of Ti) are absorbed, a K-shell electron is ejected. In a solid material, the electron wave can be reflected from neighboring atoms and interfere with the outgoing electron wave. For different photon energies, the energy (and hence the wavelength) of the ejected electron will vary and so will the phase difference between the two waves. Thus, the interference translates into modulations in the cross section for photon absorption (i.e., the opacity). The period of the modulations is clearly related to the inverse of the interatomic distance and thus yields the density. The rate of decay of the modulations depends mostly on the temperature because at higher temperatures the ion-vibration amplitude increases, which causes a random phase shift of the reflected electron waves.

The basic theory yields the following expression for $\chi(k)$:

$$\chi(k) = \sum_j N_j F_j(k) \exp\left[-2\sigma^2 k^2 - 2R_j/\lambda(k)\right]$$

$$\times \sin\left[2kR_j + \phi_j(k)\right]/kR_j^2, \qquad (3)$$

where N_j is the number of atoms surrounding the absorbing atom at a distance R_j (N_1 = 12 in Ti). The sum over j relates to the various shells of atoms around the photo-absorbing atom, in increasing distances. The backscattering amplitude $F_j(k)$ and phase-shift factor $\phi_j(k)$ for titanium were taken from the detailed calculations by Teo and Lee;[11] the mean free path of the ejected electron in titanium, $\lambda(k)$, was taken from the calculations of Blanche *et al.*[10] The vibration amplitude σ^2 (the Debye-Waller factor) and the interatomic distances R_j are treated as adjustable parameters in fitting the experimental EXAFS spectrum to Eq. (3). The distances R_j (in particular R_1) yield the density of the absorber. As discussed below, σ^2 depends on both the temperature and the density; once the density is determined from R_1, the temperature can then be determined from σ^2. Equation (3) shows that the oscillations decay with increasing k, even if σ^2 were negligibly small. For the temperatures of interest here, however, the decay is dominated by σ^2. In addition, an adjustable shift Δ is introduced[12] in the K-edge energy because of solid-state effects at energies close to the edge. Equation (3) is based on some simplifying assumptions (such as plane rather than spherical electron waves and neglect of multiple scattering). More advanced theories[13–15] include such effects, but such improvements are not essential here because the shock compression will change the interatomic distance appreciably; thus a highly precise determination of the R_j's is not required.

We next fit the experimental EXAFS spectrum to Eq. (3). The customary procedure is to work with the function $k\chi(k)$ [or even $k^3\chi(k)$] rather than $\chi(k)$. By doing so we place less weight on the low-k part of the spectrum, where the theory is uncertain. Also, to simplify the fitting, we use only the first term (j = 1) in Eq. (3). The equivalent experimental spectrum is obtained in the following manner. First, the experimental spectrum is Fourier transformed to the R space. The amplitude of the Fourier transform of $\chi(k)$ gives the charge distribution around an absorbing Ti atom.[1] Simply put, a constructive interference occurs when the interatomic distance equals an integer multiple of half the electron wavelength. Figure 86.54 shows this distribution for the two consecutive laser shots analyzed in this article. The distribution is seen to be reproducible, and it agrees well with the published data on Ti obtained with synchrotron radiation.[10,15] The major peak is due to the nearest neighbors around the absorbing atom, whereas the minor peak is due to the next shell of neighboring atoms.

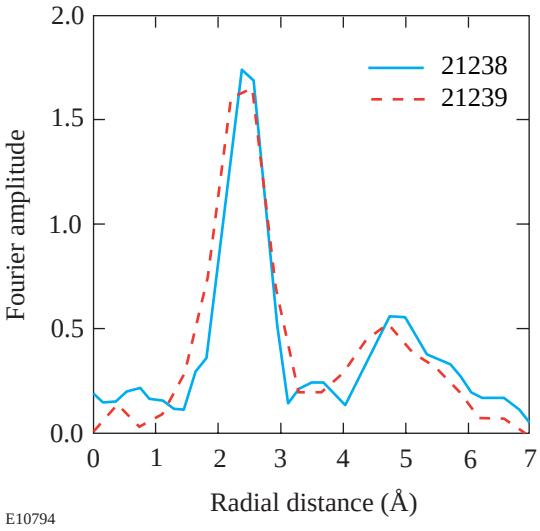

Figure 86.54
Amplitude of the Fourier transform of the EXAFS spectrum $\chi(k)$ for two consecutive laser shots. The transform corresponds to the charge distribution around the photon-absorbing Ti atom. The weaker peak is particularly sensitive to reduction in short-range order due to melting.

In addition to crystalline materials, EXAFS has been measured in amorphous materials[2,3] as well as in liquids.[4–6] As compared with crystals, the amplitude of modulations in the absorption coefficient is lower; in addition, in the R space, the farther-shell peaks are reduced more than the nearest-neighbor peak. This provides a method for detecting melting. Of particular importance in these studies is the demonstrated ability to observe the minor peak since it is more sensitive to melting or to any change in short-range order. The main peak in Fig. 86.54 is selected by multiplying the distribution by a super-Gaussian filter centered on that peak. Finally a transform back to the k space is performed. This procedure is sufficient for determining the temperature and density. The range of 2 to 10.5 Å^{-1} was used to analyze $k\chi(k)$. Below 2 Å^{-1} the curve is negligibly small; above $k \sim 10.5$ Å^{-1} the EXAFS spectrum is limited by noise.

Figure 86.55 shows the best fit, with R_1 = 2.9 Å, σ^2 = 0.0049 Å^2, and Δ = –13 eV. These values agree with the results found for Ti in synchrotron-radiation experiments.[15] The experimental spectrum $k\chi(k)$ had to be multiplied by a factor ~1.8 to normalize it to the theoretical spectrum. This is consistent

with what is found in other EXAFS studies:[16] Rehr *et al.*[16] have shown that the relaxation of bound electrons that accompanies the ejection of *K*-shell electrons reduces the EXAFS amplitude from Eq. (3) by about a factor of 2. The quality of the fit can be improved if more-sophisticated versions of the theory are used. As explained above, however, this is not required in these studies.

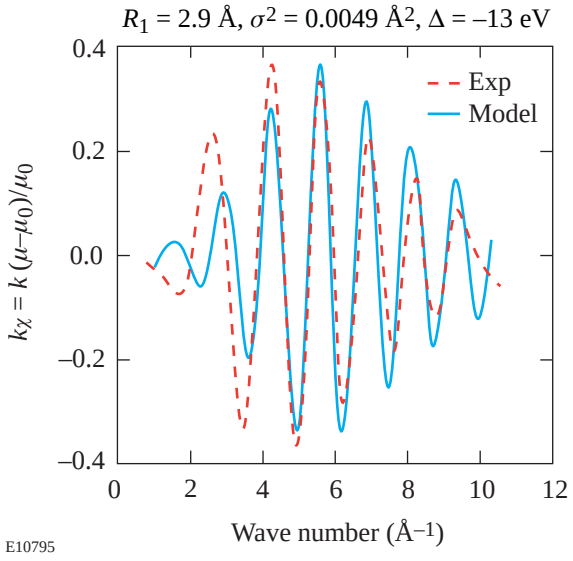

Figure 86.55
Fitting the model [Eq. (3)] to the observed EXAFS $k\chi(k)$ spectrum. Shown are the parameter values giving the best fit. The interatomic distance R_1 depends on the density, and the Debye–Waller factor σ^2 depends mostly on the temperature. Δ is an adjustable shift applied to the *K*-edge energy to account for solid-state effects.

EXAFS Visibility

1. Dependence of σ^2 on Temperature and Density

As seen from Eq. (3), when the temperature (and thus σ^2) increases, the EXAFS modulations decay faster with k and may become useless for diagnosing the target. To determine the useful temperature range for EXAFS observation we use the calculated dependence[17] of σ^2 on temperature:

$$\sigma^2 = \frac{3\hbar^2}{Mk\Theta_D}\left[(1/4)+(T/\Theta_D)^2\int_0^{\Theta_D/T}\frac{x\,dx}{e^x-1}\right], \qquad (4)$$

where M is the atomic mass. Equation (4) was derived using a Debye model of lattice oscillations in a cubic, perfect crystal. It assumes harmonic oscillations so its validity is restricted to low temperatures. It also assumes uncorrelated vibrations of the absorbing and neighboring atoms. This correlation gives rise to an additional term[17] in Eq. (4), which we have neglected. Studies of the correlation[18,19] show that it reduces σ^2 by a about a factor ~1.6 around room temperatures; this correction factor was incorporated in subsequent calculations at all temperatures. Figure 86.56 shows the dependence of the corrected σ^2 on temperature for Ti at solid density. At room temperature the value of σ^2 (~0.005 Å^2) agrees with the value found from the present experiment (Fig. 86.55), which also agrees with the results of synchrotron experiments on Ti.[10]

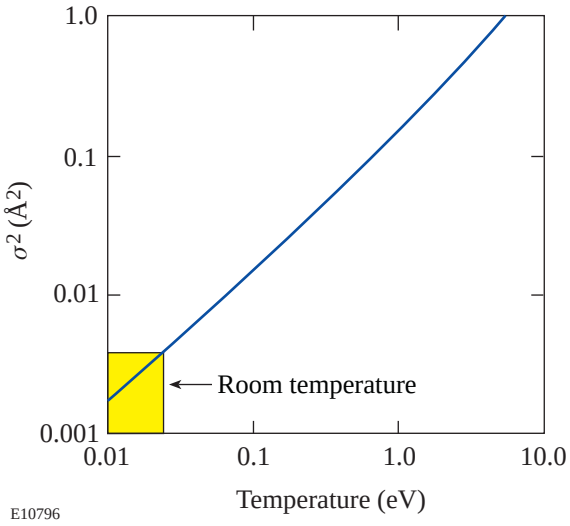

Figure 86.56
The dependence of the vibration amplitude σ^2 (corrected for correlation) on temperature for solid Ti density.

Although the increased temperature due to the shock increases σ^2 and reduces the EXAFS visibility, the increased density behind the shock *decreases* σ^2 because σ^2 depends on T/Θ_D and Θ_D increases with density. The latter can be understood by noting that Θ_D is related to k_D, the maximum wave number of phonon vibrations, which changes as R^{-1}; thus, shock compression reduces R and increases Θ_D.

The density dependence of Θ_D can be determined from an empirical model[20] due to Cowan, in terms of the nuclear charge Z and the atomic weight A. The result is

$$k\Theta_D = \left[1.68/(Z+22)\right]\left[\xi^{b+2}/(1+\xi)^2\right]\text{eV}, \qquad (5)$$

where

$$b = 0.6\,Z^{1/9},\ \xi = \rho/\rho_{ref},\ \rho_{ref} = \left(A/9Z^{0.3}\right)\text{g/cm}^3. \qquad (6)$$

Figure 86.57 shows the dependence of the Debye temperature of Ti on the density; ρ_s is the solid density. At solid density Θ_D of Ti is 0.0366 eV;[21] the model overestimates this value by about 15%, so we reduce the model-calculated Θ_D by that factor. Because σ^2 depends on both temperature and density, both parameters must be determined as a function of shock strength in order to assess the expected EXAFS visibility.

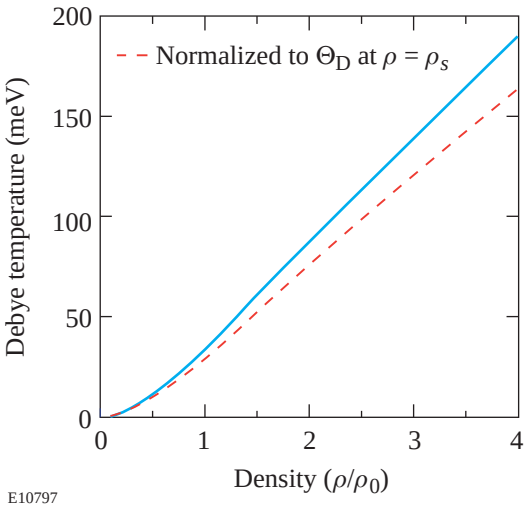

Figure 86.57
Calculated dependence of the Debye temperature of Ti on compression using Cowan's model.[20] The dashed curve is normalized to the known Θ_D of Ti at solid density ρ_s.

2. Dependence of Density and Temperature on Shock Strength

In future experiments the Ti foil will be embedded in a double CH layer and driven by a single laser beam, while still backlit by a spherically imploded target. The front CH layer will be thick enough to ensure that no burnthrough occurs before the shock traverses the Ti layer; the role of the rear-surface CH layer is to avoid extraneous effects due to unloading of the shock when arriving at the target–vacuum interface. The parameter space where high-amplitude EXAFS oscillations can be expected to be observed is now estimated. As seen above, both temperature and density achieved by shock compression of Ti as a function of laser irradiance must be determined by (a) using the experimentally known[22] Hugoniot of Ti and (b) simulating the interaction with the 1-D code *LILAC*. In these simulations a 10-μm-thick Ti layer was assumed to be coated on each side by a 5-μm-thick CH layer and irradiated by a 1-ns square pulse of various powers. These simulations also determine the uniformity behind the shock over a thick Ti layer. This requirement is essential for an unequivocal interpretation of the EXAFS results. The *LILAC* simulations (see examples in Fig. 86.58) show that when the shock arrives at the back surface of the Ti layer, the temperature and density within the layer are uniform to within ±10% and the Ti layer is unaffected by rarefaction.

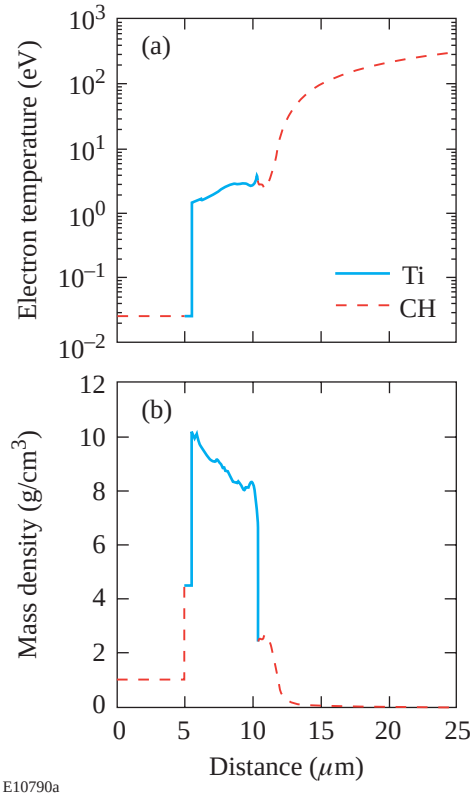

Figure 86.58
Example of *LILAC* simulations of a shock wave in a 10-μm-thick Ti layer sandwiched between two 5-μm-thick CH layers, produced by a 1-ns square pulse at 20 TW/cm^2. The density and temperature profiles are shown for the instant the shock arrives at the back surface of the Ti layer.

LILAC was run for a series of increasing values of laser intensity, and in each case the density and temperature (averaged over the Ti layer) were determined at the instant the shock arrived at the back surface of the Ti layer. The results are shown in Fig. 86.59 (for the density) and in Fig. 86.60 (for the temperature) as points marked by the value of laser intensity in TW/cm^2. In parallel to these simulations the density and temperature were determined from experimentally known data. In Fig. 86.59, the red curve shows the measured principal Hugoniot of Ti.[22] Although the curves are shown over a wide pressure range, the main interest here is in their low-pressure portion; thus, the melting temperature of Ti at solid density is at 1941°K, or 0.167 eV.

Using the Hugoniot curve, we now determine the temperature in the shocked Ti layer. First, from the Rankine–Hugoniot relation

$$E - E_0 = (P/2)\left[(1/\rho_0) - (1/\rho)\right] \tag{7}$$

we determine the energy increase due to the shock. Here E, P, and ρ are the energy per unit mass, the pressure, and the density behind the shock front, and the subscripted quantities refer to the region in front of the shock front (P_0 = 0 was assumed). From the energy increase E–E_0 we calculate the temperature behind the shock front, using the quotidian equations of state for ions and electrons described in Ref. 20. For the ions, the energy per ion above Θ_D is given by

$$E_i = 3kT\left[1 + \left(u^2/20\right) - \ldots\right], \quad u = \Theta_D(\rho)/T. \tag{8}$$

For temperatures much higher than Θ_D, as is the case here, this reduces to $E_i = 3\,kT$ (the Dulong–Petit law). For the electrons, a modifed Fermi–Thomas (FT) equation of state is used.[23] The FT theory at low temperatures yields too high an electron pressure (~Mbars) because the bonding between adjacent atoms is neglected and must be corrected. In a convenient semi-empirical correction method devised by Barnes[24] an expression for the bonding energy ΔE (negative for densities higher than solid) is added to the electron energy. ΔE (energy per cm^3) is given by

$$\Delta E = E_0\left\{1 - \exp\left[b - b\left(\rho_s/\rho\right)^{1/3}\right]\right\}, \tag{9}$$

where ρ_s is the solid density and E_0 and b are adjustable parameters. To be consistent with thermodynamic relations, this change in energy must be accompanied with a change in pressure given by

$$\Delta p = \rho^2 \frac{\delta \Delta E}{\delta \rho} = -\left(\frac{E_0 b \rho_s}{3}\right)\left(\frac{\rho}{\rho_s}\right)^{2/3} \exp\left[b - b\left(\frac{\rho_s}{\rho}\right)^{1/3}\right], \tag{10}$$

and the revised bulk modulus becomes

$$B = \rho\left(\delta p_e/\delta\rho\right)_{\rho_s} - (b+2)\left(E_0 b \rho_s\right)/9. \tag{11}$$

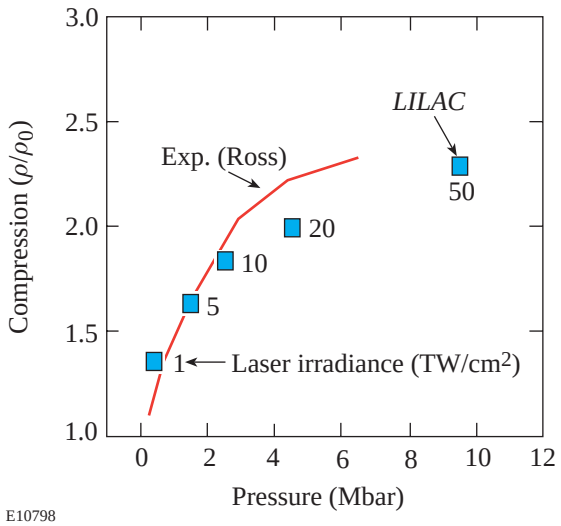

Figure 86.59
Experimentally determined[22] principal Hugoniot in Ti (red curve). The points were obtained from *LILAC* code simulations of a shock created when a laser of the shown irradiance (in TW/cm^2) irradiated the buried-Ti target.

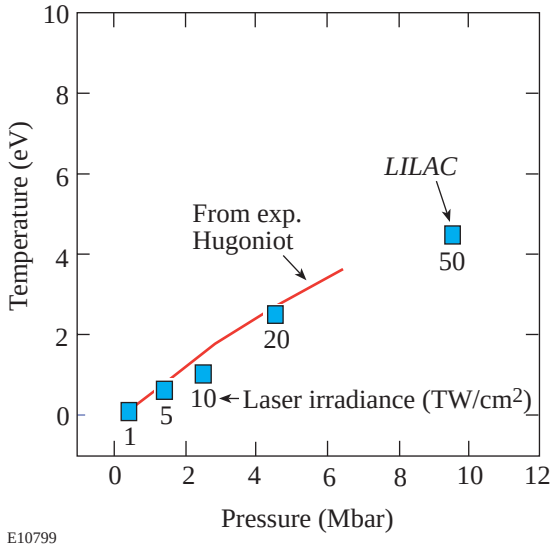

Figure 86.60
Temperature behind the shock as a function of the shock pressure in Ti (red curve) calculated from the known principal Hugoniot and the corrected Fermi–Thomas equation of state. The points were obtained from *LILAC* code simulations of a shock created when a laser of the shown irradiance (in TW/cm^2) irradiated the buried-Ti target.

Here we neglected the ion pressure p_i. Using these two relations for the energy and the pressure, E_0 and b are found from the following two conditions: (a) the corrected pressure $p + \Delta p$ (where p is the Fermi–Thomas pressure) at solid density and $T = 0$ should be 0, and (b) B should agree with the known bulk modulus at normal temperature and density (for Ti, B equals[25] 1.1×10^{12} dyn/cm^2). We now add ΔE from Eq. (9), with E_0 and b thus determined, to the Fermi–Thomas energies[23] for Ti, using for the latter the fitting expressions worked out by Bell.[26] Using Eq (7), the energy along the experimental Hugoniot (Fig. 86.59) can be calculated. We now equate these energy values with the revised Fermi–Thomas energies. Since these energies depend on density and temperature, using the known densities (Fig. 86.59), we can now search for the temperatures along the Hugoniot. The results are shown as a red curve in Fig. 86.60. Good agreement between the *LILAC* simulations and the experiment-based model is seen in Figs. 86.59 and 86.60, especially for the low-pressure range of relevance in this study.

3. EXAFS Visibility as a Function of Shock Strength

Finally, the vibration amplitude σ^2 can be determined as a function of shock strength from Figs. 86.59 and 86.60, using Eqs. (4) and (5). The results, over the range of pressures of the experimental Hugoniot, are shown in Fig. 86.61. Using Eq. (3) we can show that significant EXAFS modulations can be seen whenever $\sigma^2 \lesssim 0.1$, so Fig. 86.61 indicates that such modulations in forthcoming shock experiments are expected to show significant amplitude. It should be noted, however, that the density affects the EXAFS visibility directly, in addition to affecting it through σ^2. Thus, at a higher density the modulation amplitude increases because of the appearance of the interatomic distance R in the denominator of Eq. (3). On the other hand, at a higher density the period of the EXAFS oscillations increases, and there are fewer oscillation periods within the range of k where their amplitude is significant. To demonstrate these effects, the EXAFS spectrum calculated from Eq. (3) was plotted in Fig. 86.62 for two conditions: (a) $\sigma^2 = 0.04$ Å^2 at solid density. From Fig. 86.56 this corresponds to $T \sim 0.25$ eV, just above the melting point. Significant EXAFS modulations are seen for this case. (b) $\sigma^2 = 0.1$ Å^2 at 2.5× solid density. This represents an extreme case where σ^2 is higher than what will be encountered in these experiments (see Fig. 86.61). The EXAFS spectrum in this case is only marginally useful, especially for determining the density; however, it can still provide a good indication of the temperature. Finally, in calculating the expected EXAFS spectrum we have not included the effect of noncrystallinity, which would modify Eq. (3). Experiments on EXAFS in molten metals [see, e.g., Ref. 6(b)] show that the modulation amplitude upon melting is reduced by about a factor of 1.5. Thus, the conclusions reached above should not change significantly when melting is included in the analysis.

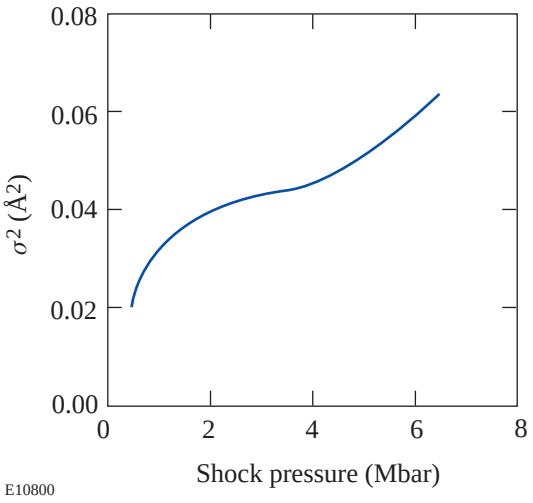

Figure 86.61
The vibration amplitude σ^2 as a function of shock strength, calculated from Figs. 86.59 and 86.60, using Eqs. (4) and (5).

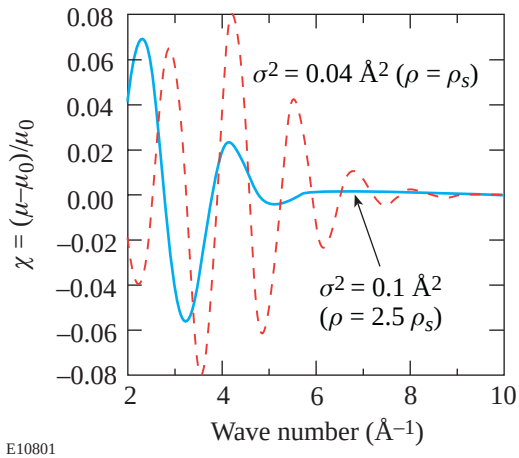

Figure 86.62
Demonstration of the effects of σ^2 and the density on the EXAFS spectrum in Ti. The density affects the spectrum both directly and through σ^2.

ACKNOWLEDGMENT

This work was supported by the U.S. Department of Energy Office of Inertial Confinement Fusion under Cooperative Agreement No. DE-FC03-92SF19460, the University of Rochester, and the New York State Energy Research and Development Authority. The support of DOE does not constitute an endorsement by DOE of the views expressed in this article.

REFERENCES:

1. P. A. Lee *et al.*, Rev. Mod. Phys. **53**, 769 (1981).
2. M. C. Ridgway *et al.*, Nucl. Instrum. Methods Phys. Res. B **147**, 148 (1999).
3. D. E. Sayers, E. A. Stern, and F. W. Lytle, Phys. Rev. Lett. **27**, 1204 (1971).
4. Y. Katayama, O. Shimomura, and K. Tsuji, J. Non-Cryst. Solids **250–252**, 537 (1999).
5. K. Tamura *et al.*, J. Non-Cryst. Solids **150**, 351 (1992).
6. E. D. Crozier, in *EXAFS Spectroscopy: Techniques and Applications*, edited by B. K. Teo and D. C. Joy (Plenum Press, New York, 1981), Chap. 6, p. 89; E. D. Crozier and A. J. Seary, Can. J. Phys. **58**, 1388 (1980).
7. R. W. Eason *et al.*, J. Phys. C, Solid State Phys. **17**, 5067 (1984); B. A. Shiwai *et al.*, Laser Part. Beams **10**, 41 (1992).
8. B. Yaakobi, F. J. Marshall, D. K. Bradley, J. A. Delettrez, R. S. Craxton, and R. Epstein, Phys. Plasmas **4**, 3021 (1997).
9. F. J. Marshall, T. Ohki, D. McInnis, Z. Ninkov, and J. Carbone, Rev. Sci. Instrum. **72**, 713 (2001).
10. G. Blanche *et al.*, Ultramicroscopy **50**, 141 (1993).
11. B.-K. Teo and P. A. Lee, J. Am. Chem. Soc. **101**, 2815 (1979).
12. See Ref. 1, Sec. IV(B); Ref. 15, p. 6358.
13. P. A. Lee and J. B. Pendry, Phys. Rev. B **11**, 2795 (1975).
14. J. J. Rehr and R. C. Albers, Rev. Mod. Phys. **72**, 621 (2000).
15. A. Balzarotti, M. De Crescenzi, and L. Incoccia, Phys. Rev. B **25**, 6349 (1982).
16. J. J. Rehr *et al.*, Phys. Rev. B **17**, 560 (1978); see also Ref. 1, Sec. III(G).
17. G. Beni and P. M. Platzman, Phys. Rev. B **14**, 1514 (1976).
18. R. B. Greegor and F. W. Lytle, Phys. Rev. B **20**, 4902 (1979).
19. G. Dalba and P. Fornasini, J. Synchrotron Radiat. **4**, 243 (1997).
20. R. M. More *et al.*, Phys. Fluids **31**, 3059 (1988).
21. R. E. Bolz and G. L. Tuve, eds. *CRC Handbook of Tables for Applied Engineering Science*, 2nd ed. (CRC Press, Boca Raton, FL, 1973), Chap. 2.2, p. 231.
22. M. Ross, Rep. Prog. Phys. **48**, 1 (1985).
23. R. Latter, Phys. Rev. **99**, 1854 (1955).
24. J. F. Barnes, Phys. Rev. **153**, 269 (1967).
25. G. V. Samsonov, ed. *Handbook of the Physicochemical Properties of the Elements* (IFI/Plenum, New York, 1968), Chap. VI, p. 397.
26. A. R. Bell, Rutherford and Appleton Laboratories, Chilton, Didcot, Oxon, England, Report RL-80-091 (1980).